Cold Regions Science and Technology 211 (2023) 103875

Contents lists available at ScienceDirect

Cold Regions Science and Technology

journal homepage: www.elsevier.com/locate/coldregions

Microphone recording of flexural waves for estimation of lake ice thickness

Rowan Romeyn *, Alfred Hanssen

Department of Geosciences, University of Tromsø – The Arctic University of Norway, Tromsø 9037, Norway

ARTICLE INFO

Keywords:
Non-destructive testing
Non-contact non-destructive testing
Air-coupled flexural wave
Thin floating plate
Leaky wave
Floating ice sheet
Bearing capacity
Dispersive
Flexural wave
Microphone

ABSTRACT

In this study we took an intentionally low-tech approach, aiming to estimate key physical parameters of lake ice using a single, inexpensive microphone. We consider this approach highly relevant to the issue of transport safety and the relatively high number of accidents involving breakthrough failure of thin ice underlines the importance of this topic. We conducted a range of experiments on three frozen lakes in the Tromsø region of Northern Norway and found that the monochromatic air-coupled flexural wave was a robust feature of impulsively excited frozen lakes. Ice thickness was estimated via a closed form solution that only depends on the measured monochromatic frequency of the air-coupled flexural wave and a set of assumed physical parameters for the ice, air and water. We discuss the impact of uncertainty in the assumed parameters on estimated ice thickness and bearing capacity, finding the uncertainty to be quite small, particularly when physical observation of ice type or drilled thickness are available to constrain the assumed Young's modulus of the ice. Ice thicknesses estimated from air-coupled flexural waves were typically within 5–10% of ice thickness measured in holes drilled in the vicinity of the microphone for both artificial sources including hammer strikes, jumping and tapping with ice skates and natural ice quakes. The thickness estimates were also similarly accurate whether the microphone was resting on the ice, placed on land along the shoreline or handheld. We also showed that it is possible to record the dispersive ice flexural wave using a microphone, particularly when it was resting on the ice surface. Since thickness was constrained by the air-coupled flexural wave, we were able to estimate the propagation distance, corresponding to the horizontal offset between source and microphone, by inversion of the time dispersed arrival of the chirp signal corresponding to the ice flexural wave. We also demonstrated that a microphone can record inharmonic monochromatic overtones of the air-coupled flexural wave, that were linked to the geometry and boundary conditions of the frozen lakes using finite element modal analysis. This study leads us to conclude that a simple microphone can be a powerful tool giving a surprising amount of information on the lake-ice system. Using a microphone to record air-coupled flexural waves appears to be a promising additional tool for evaluation of ice conditions, convenient enough that it could substantially increase the availability of timely and accurate information on ice thickness and thereby contribute to safer travel on floating ice.

1. Introduction

Continuous ice of sufficient thickness is the main requirement to support a given load and allow safe travel across floating ice (Masterson, 2009). Accidents associated with travel across thin ice with insufficient load bearing capacity occur with unfortunate regularity and result in a significant number of fatalities. This is illustrated by Fig. 1, which provides a summary of accidents involving floating ice in Norway over the period 2006–2023. The vast majority of these accidents should be considered avoidable, had timely and accurate information on ice thickness and bearing capacity been available. In this context, air-coupled flexural waves recorded with simple and inexpensive microphones could lead to the possibility to develop convenient and easily accessible means to estimate ice thickness and avoid travel on unsafe ice.

When floating ice is loaded, it bends and develops flexural stress across its vertical cross section, with the basal surface experiencing tension and the upper surface experiencing compression (Masterson, 2009). Since ice is weaker under tension than it is under compression, the critical stress is the tensile stress at the base of the ice directly under the load and failure by cracking occurs when this critical stress exceeds the tensile strength of the ice (Masterson, 2009). If loading continues, the initial basal tensile crack develops into a series of radial cracks penetrating the ice thickness and propagating outwards to some distance

* Corresponding author.
E-mail address: rowan.romeyn@uit.no (R. Romeyn).

https://doi.org/10.1016/j.coldregions.2023.103875
Received 26 January 2023; Received in revised form 4 April 2023; Accepted 18 April 2023
Available online 20 April 2023

outside the loaded area. As loading continues further, a circumferential crack pattern linking the edges of the radial cracks also forms and complete breakthrough occurs (Masterson, 2009). The amount of stress developed in the ice is proportional to the flexural displacement, or strain, of the ice under load. Over short timescales ice deforms elastically under load, while inelastic creep also contributes to deformation over longer timescales. The elastic deformation of a homogeneous ice plate under a given load is proportional to its flexural stiffness, D, given by

$$\mathrm{D} = \frac{Eh^3}{12(1-\sigma^2)} \tag{1}$$

where E is Young's modulus, h is the plate thickness, and σ is Poisson's ratio. The flexural stiffness depends primarily on the cubed ice thickness, and justifies the statement that ice of sufficient thickness is the main requirement to support a given load. For a concentrated point load on an un-cracked plate, the maximum elastic deflection directly beneath the load, δ_m, can be expressed as (e.g., Beltaos, 2002; Kerr, 1976)

$$\delta_m = \frac{P}{8\sqrt{D\rho_w}} \tag{2}$$

where P is the force exerted by the load and ρ_w is the density of the water supporting the plate. The maximum deflection at failure, δ_{mf}, may be approximated as

$$\delta_{mf} = \gamma h \tag{3}$$

where $\gamma \approx 0.5$ is an empirical constant (Beltaos, 2002; Sodhi, 1995). Correspondingly, the breakthrough load, P_f, is given by

$$P_f = 8\gamma h\sqrt{D\rho_w} \tag{4}$$

Thus, the critical ice thickness, h_f, at a given load, P, may be expressed as

$$h_f = \left[\frac{3}{16}\frac{P^2(1-\sigma^2)}{\gamma^2\rho_w E}\right]^{1/5} \tag{5}$$

Importantly, these expressions correspond to the instantaneous breakthrough condition (e.g. Beltaos, 2002). In reality, inelastic creep also contributes to deflection (Beltaos, 1978), particularly for slowly moving or stationary loads exerting force on the plate over time so that breakthrough may occur also for ice thicker than the limiting case of instantaneous breakthrough. As an example, with ice temperature of −5 °C the deflection due to creep corresponds to ~10% of the elastic deflection after five seconds and ~ 40% after 8 min (Beltaos, 2002; Sinha and Cai, 1996). When calculating safe travel conditions, safety factors and tolerance for spatially varying ice conditions should also be accounted for. When ice bearing capacity is assessed via holes drilled through the ice, it has been common practice to ignore or downgrade the thickness of poor-quality ice based on qualitative properties (e.g., Hayley et al., 2013) like colour (white vs. blue ice) or texture (slushy, water lenses, wet cracks, poor interlayer bonding, etc.), which complicates the evaluation of bearing capacity by direct sampling.

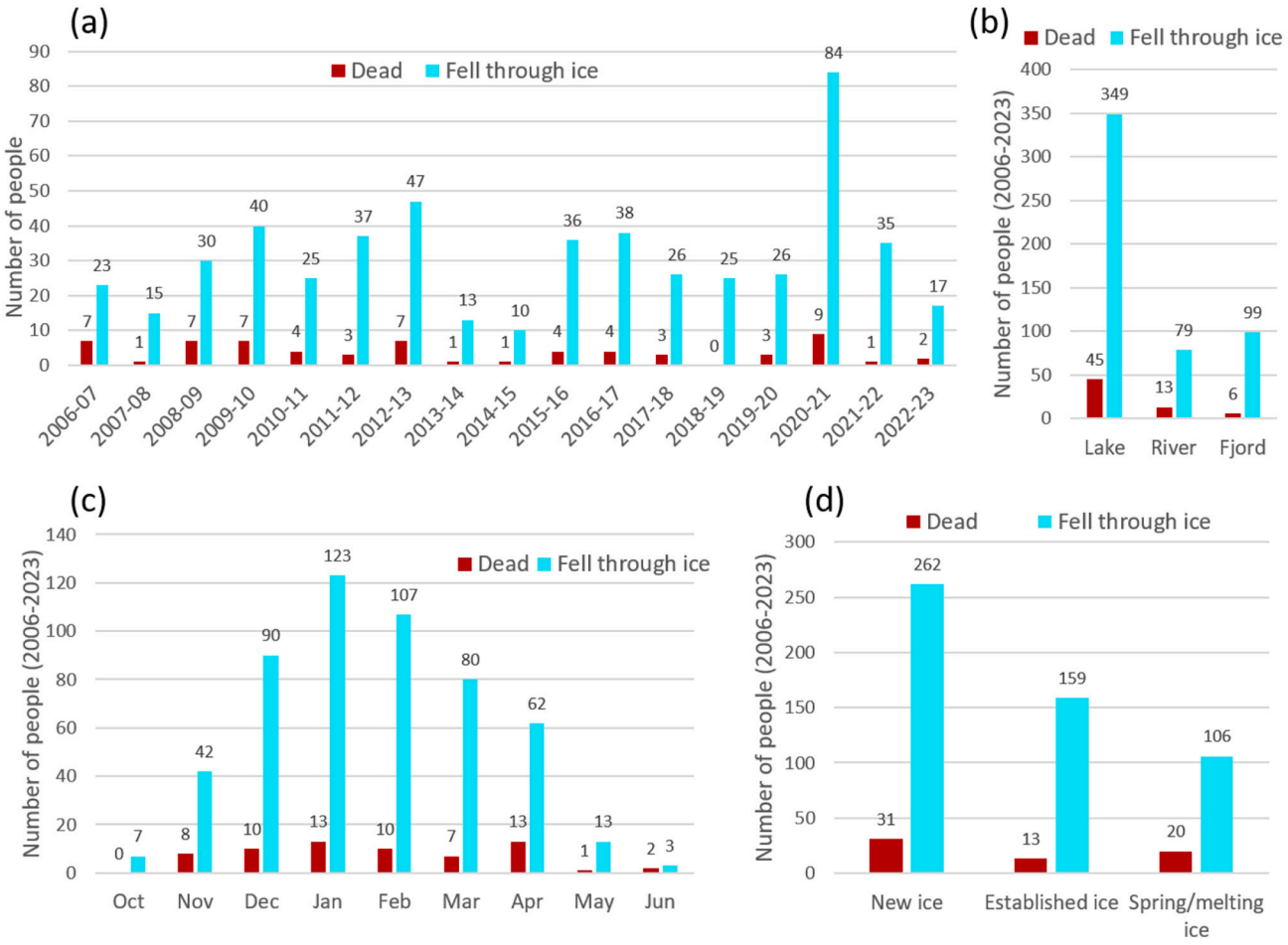

Fig. 1. (a) Number of people involved in reported accidents on floating ice in Norway (including Svalbard) between 2006 and January 2023, (b) the type of water body involved, (c) summary of accident seasonality and (d) the type of ice involved. Data from NVE (2023) based on collated reports published in traditional and social medias and incidents registered in the "Varsom Regobs" database (regobs.no). Persons falling through thin ice who were well prepared with the appropriate knowledge and equipment required to enact effective self-rescue are not included in these statistics.

Impulsive loading of a floating ice plate leads to the propagation of flexural waves whose propagation characteristics are strongly influenced by the flexural stiffness of the ice. Flexural waves propagating in a floating plate are a class of guided elastic waves analogous to bending waves in rods or beams and the Lamb waves of a free plate. Greenhill (1886) published one of the earliest mathematical descriptions of flexural waves in a floating ice sheet and several studies have used the dispersion of ice flexural waves to estimate ice elastic parameters. Of these, we highlight in particular the early work of Ewing and Crary (1934), the study of Yang and Yates (1995) that advanced the use of transform methods, and the recent extension to the paradigm of passive seismic techniques of Marsan et al. (2012), Moreau et al. (2020a) and Moreau et al. (2020b). An alternative approach based on recording the monochromatic air-coupled flexural wave set up between horizontally propagating pressure waves in air and flexural waves in the solid having phase velocity equal to the speed of sound in air and was first identified by Press et al. (1951) and recently elaborated on by Romeyn et al. (2021). Since the phase velocity of the air-coupled flexural wave is fixed to the speed of sound in air, the monochromatic frequency recorded at a single sensor constrains the ice flexural stiffness, where studies of ice flexural waves typically employ arrays of sensors to allow flexural wave velocities to be measured as a function of frequency. Since ice bearing capacity is related to flexural stiffness and flexural waves respond to the average properties across the vertical profile (Timco and Weeks, 2010), flexural waves may provide an effective means to estimate the effective flexural stiffness and bearing capacity.

Studies of flexural waves in floating ice, such as those mentioned in the previous paragraph, have primarily employed geophones to measure movements of the ice surface and infer wave propagation characteristics. An innovative recent study by Nziengui-Bâ et al. (2022) has also demonstrated the drone assisted deployment of a fibre optic cable coupled with distributed acoustic sensing as an alternative acquisition system. This system is better suited to deployment on thin early-season ice that is not safe to traverse than more traditional acquisition systems employing geophones installed by hand. The air-coupled flexural wave also gives the potential for flexural wave acquisition using a microphone recording pressure waves in the air above the ice, which was demonstrated by Romeyn et al. (2021), although their main focus was on geophone data. Recording of air-coupled flexural waves with a microphone above the ice also shares a connection to an innovative research front within non-destructive testing (NDT), namely non-contact air-coupled non-destructive evaluation systems (e.g., Bjurström and Rydén, 2019; Harb and Yuan, 2018). These systems are of interest to NDT since they avoid having to bond sensors directly to the surface which can increase operational efficiency in a production scenario involving testing of large numbers of samples (Harb and Yuan, 2018; Zhu, 2008) or while rolling continuously across the surface (Bjurström and Rydén, 2019).

The main focus of this article is to further elaborate the potential to measure flexural waves and estimate ice thickness using a single microphone. This is an extreme “low-tech” approach compared to acquisition systems consisting of arrays of geophones or drone deployed DAS cables and we aim to explore how much information can be extracted, and to what degree of accuracy, using such a low-tech system. Given that the vast majority of people carry around reasonably capable microphones at all times, in the form of smartphones, we consider this topic highly relevant to the problem of increasing the accessibility of timely and accurate information on ice thickness and bearing capacity, promoting safer travel across floating ice.

2. Study area and data acquisition

In this study we conducted a series of experiments, from late November 2022 to early December 2022, aiming to record the flexural wavefield of frozen lakes near Tromsø, Northern Norway, using a microphone. The study locations considered in this article are illustrated in Fig. 2.

The smallest lake, Langvannet (Fig. 2b), is a short walking distance from the University of Tromsø campus and was mostly used to conduct controlled experiments using artificial sources. No natural icequakes were observed at Langvannet, although surficial cracking suggests that this was simply due to the timing of experiments during periods of stable temperature. There was also significantly more background noise at this location due to the proximity to roads, air traffic and other human activity. The two lakes on Kvaløya, Storvatnet (Fig. 2c) and Kråkskarvatnet (Fig. 2d), provided an opportunity to investigate flexural waves excited by natural icequakes, and the lower ambient noise levels at these locations also facilitated the recording of these signals. Studying different lakes also allowed measurements corresponding to different ice conditions and thicknesses to be obtained. All three lakes were snow-free, while not within the scope of this study, snow insulates the ice from rapid swings in air-temperature, presumably decreasing the probability of thermal stress related icequakes. Snow is also assumed to have a damping effect on the coupling between flexural waves in ice and acoustic waves in air.

The experiments were designed to be low-tech, using only inexpensive household equipment or tools available at a typical hardware store. Flexural waves were excited using artificial sources, consisting of hammer blows, jumping or tapping with ice skates and natural sources, i.e., icequakes caused by surficial ice cracking due to rapid changes in air temperature. Jumping produced signals with the largest amplitudes, but gave a double source due to the fact that each foot impacts the ice at a slightly different instant. Striking the ice with a typical household hammer weighing 580 g was therefore the preferred artificial impulse. Data was recorded using an Olympus LS-P4 stereo microphone, which records frequencies from 20 Hz to 20 kHz, using the loss-less compressed FLAC format with a sampling frequency of 44.1 kHz. Since the microphone stereo baseline is very small (~4 cm) compared to the air-coupled flexural wavelengths (> 1 m), the mean of the two stereo channels was taken to give a single channel record.

The ice thickness was checked by drilling using a handheld power drill with a 25 mm diameter, 42 cm long auger bit and a tape measure. Water depth was also measured when less than the 3–5 m length of the two tape measures used. Positions were recorded using a smartphone GPS and air temperatures were recorded at the start, end and sporadically during the experiments with an alcohol thermometer.

3. Theory

In this study we focus on the linear dispersion relation of the flexural wave field in a floating elastic plate of thickness, h, and density, ρ, with infinite horizontal extent, resting on an incompressible inviscid fluid of finite depth, H, and density, ρ_w, and neglecting longitudinal plate stresses due to the action of wind or pressure gradients in the ice or water. It has been well documented that the dispersion relation of this system is given by (e.g. Romeyn et al., 2021; Squire et al., 1996)

$$\omega(k) = \left[\frac{\alpha k^5 + gk}{\beta k + coth(kH)}\right]^{1/2} \tag{6}$$

where $\omega(k)$ is the angular frequency at wavenumber k, $g = 9.81\ \mathrm{ms}^{-2}$ is the gravitational acceleration, $\alpha = D/\rho_w$, (and)

$$\beta = h\rho/\rho_w$$

The flexural wave phase velocity is given by

$$\nu_\varphi(k) = \frac{\omega(k)}{k} \tag{7}$$

and the group velocity is given by

$$\nu_g(k) = \frac{\partial\omega(k)}{\partial k} \tag{8}$$

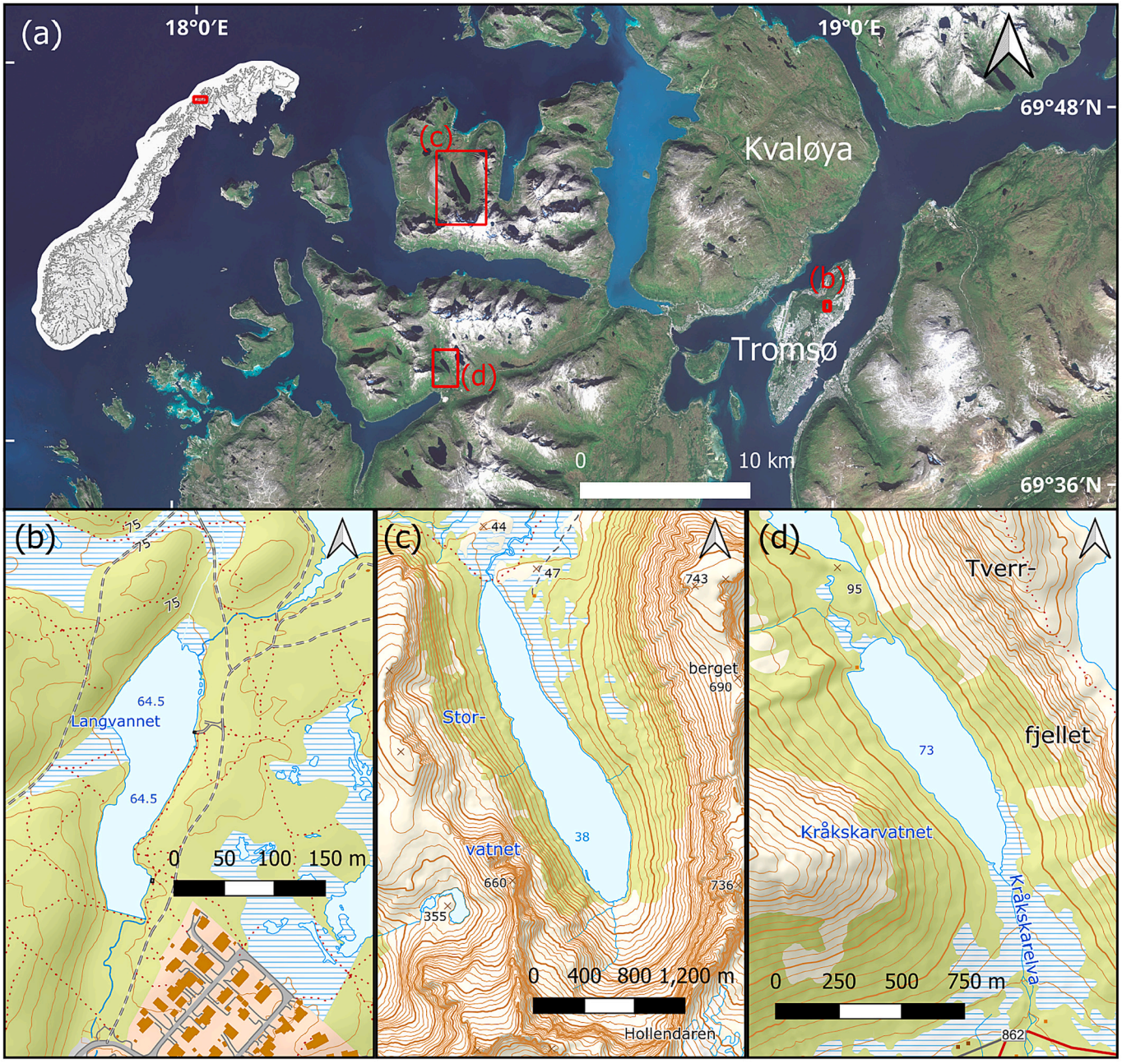

Fig. 2. (a) Orthophoto composite of the study area, on Tromsø and Kvaløya in Northern Norway. Inset topographic maps show the three frozen lakes (b) Langvannet, (c) Storvatnet and (d) Kråkskarvatnet, where the flexural wave experiments reported in this study were conducted on 23rd of November, 28th of November and 2nd of December 2022, respectively. Orthophoto from ©norgeibilder.no and topographic maps from ©Kartverket, kartverket.no.

By direct differentiation of Eq. (6), we found that the group velocity can be written as

$$\frac{\partial\omega(k)}{\partial k} = \frac{\Omega(k)}{\omega(k)} \tag{9}$$

where

$$\Omega(k) = \frac{4\alpha\beta k^5 + \left(5\alpha k^4 + g\right)coth(kH) + Hk\left(\alpha k^4 + g\right)csch^2(kH)}{2[\beta k + coth(kH)]^2} \tag{10}$$

By combining Eq. (9) with Eqs. (7) and (8), we see that the flexural wave field possesses an interesting reciprocal relationship between the group velocity and the phase velocity,

$$\nu_g(k) = \frac{\Omega(k)}{k\nu_\varphi(k)} \tag{11}$$

A useful approximation appears for $kH \gg 1$, i.e., for short wavelengths and/or large water depths. In this limit, we see that

$$\omega(k) = \left(\frac{\alpha k^5 + gk}{\beta k + 1}\right)^{1/2} \text{ and } \Omega(k) = \frac{\alpha k^4(4\beta k + 5) + g}{2(\beta k + 1)^2} \tag{12}$$

which may be sufficiently accurate for many practical applications. Another useful limiting case approximation results if we remove the fluid, i.e., if we consider a plate in a vacuum. This can be achieved by rewriting Eq. (6) as

$$\omega(k) = \left[\frac{Dk^5 + g\rho_w k}{\rho h k + \rho_w coth(kH)}\right]^{1/2} \tag{13}$$

and thereafter removing the fluid by imposing $\rho_w = 0$. Then the dispersion relation simplifies to the well-known expression

$$\omega(k) = k^2\left(\frac{D}{\rho h}\right)^{1/2} \tag{14}$$

and the associated phase and group velocities become

$$\nu_\varphi(k) = k\left(\frac{D}{\rho h}\right)^{1/2} \tag{15}$$

and

$$\nu_g(k) = 2\nu_\varphi(k) \tag{16}$$

respectively. A useful property of the plate in a vacuum case is that a simple closed form expression for the frequency dependent arrival time of the envelope of the dispersive ice flexural wave, $t(\omega)$, which propagates at the group velocity, may be derived. Rearranging Eq. (14) for k and substituting, Eq. (16) can be formulated as

$$\nu_g(\omega) = 2\left(\frac{D}{\rho h}\right)^{1/4}\omega^{1/2} = \frac{x}{t(\omega)} \tag{17}$$

where x is the propagation distance. It follows that the arrival time of the envelope of the dispersive ice flexural wave is

$$t(\omega) = \frac{x}{2}\left(\frac{D}{\rho h}\right)^{-1/4}\omega^{-1/2} \tag{18}$$

We denote the angular frequency of the monochromatic air-coupled flexural wave as ω_f. The phase velocity of the air-coupled flexural wave is constrained by the speed of sound in air, c_{air}, that we assume to be adequately represented as a function of the measured air temperature, T_{air}, following the empirical relation (e.g. Kinsler et al., 2000)

$$c_{air} = 331.3 + T_{air} \times 0.606 \ \left[\mathrm{m\ s^{-1}}\right] \tag{19}$$

where the air temperature is given in degrees Celsius.

As shown by Romeyn et al. (2021), a closed-form expression for the corresponding ice thickness, h, that satisfies the full dispersion relation, Eq. (6) is given by

$$h = 2\sqrt{\frac{b}{3a}}cos\left[\frac{1}{3}cos^{-1}\left(\frac{-3\sqrt{3}}{2}a^{1/2}b^{-3/2}c\right)\right] \tag{20}$$

where $a = \frac{E\omega_f{}^5}{12\rho_w c_{air}^5(1-\sigma^2)}$, $b = \frac{\omega_f^3}{c_{air}}\frac{\rho}{\rho_w}$ and $c = g\frac{\omega_f}{c_{air}} - \omega_f{}^2 coth\left(\frac{\omega_f}{c_{air}}H\right)$.

It is important to note that ice thickness estimated with the above closed-formed expression only depends on the measured constant frequency, ω_f, and measured or assumed physical parameters for the ice, air and water.

4. Methodology

The monochromatic air-coupled flexural wave was found to be the most robust feature of the microphone recorded wavefield excited by an impulsive load on a floating ice plate. Correspondingly, the air-coupled flexural wave was used as the key constraint on the ice physical properties. In some cases, we also recorded the broadband compressional wave in air and the dispersive chirp signal of the ice flexural wave. In some cases, we also recorded inharmonic overtones of the air-coupled flexural wave. The following sections describe how physical information was extracted from the recorded wavefield.

4.1. Signal isolation and time-frequency representation

Segments of microphone recordings containing events corresponding to both artificial sources (hammer, jump, tapping with ice skate) and natural sources (icequakes) were extracted manually. Short-time Fourier-transform (STFT) spectrograms were formed using 2^{12} samples (~0.09 s), 95% overlapping Kaiser windows with shape parameter $\beta = 10$. Following the convention, the power spectral densities (PSD) were converted to dB scale to compress spectrogram dynamic range and facilitate analysis of weaker amplitude components of the wavefield. The Thomson multitaper PSD (Thomson, 1982) for each manually extracted record was also estimated, using a time-half bandwidth product of 4 and a zero-padded Fourier transform length of 8192 samples, giving improved spectral resolution compared to the STFT. Thomson's estimator utilizes a set of orthonormal data tapers called discrete prolate spheroidal sequences to control spectral leakage and stabilize the estimate through an inherent variance reduction (Hanssen, 1997), and this estimator is the optimal nonparametric power spectral estimator in terms of spectral concentration.

4.2. Air-coupled flexural wave frequency and ice thickness estimation

The air-coupled flexural frequency, ω_f, was estimated from the multitaper PSD maximum over the heuristically determined frequency range of 100–350 Hz. This frequency range reduces the potential for spectral contamination by other noise sources and corresponds to a very conservative estimate of the expected ice thicknesses. The nominal arrival time of the air-coupled flexural wave was determined by localising the maximum along the time axis of the STFT at the corresponding frequency. Thereafter, the ice thickness was estimated using Eq. (20). The speed of sound in air was estimated based on the measured air temperature according to Eq. (19). The value of Young's modulus, E, was obtained by calibration with drilled thickness, h_{drill}, using Eq. (6) rearranged as

$$E = \frac{12\rho_w(1-\sigma^2)\omega_f^2\left[\frac{\omega_f}{c_{air}}h_{drill}\frac{\rho}{\rho_w} + coth\left(\frac{\omega_f}{c_{air}}H\right) - g\frac{\omega_f}{c_{air}}\right]}{\left(\frac{\omega_f}{c_{air}}\right)^5 h_{drill}^3} \tag{21}$$

with the remaining parameters assumed to be constant, $\sigma = 0.31$, $\rho = 917\ \mathrm{kgm^{-3}}$, $\rho_w = 1000\ \mathrm{kgm^{-3}}$ corresponding to columnar fresh water ice (Sinha, 1989). Water depth, H, was measured at holes drilled through the ice up to the maximum length of the tape measure (3 m), but were consistently >1.5 m and play no practical role in the calculation for the frequency-wavenumber range encountered in this study.

4.3. Air wave arrival time and origin time

To emphasize broadband, non-dispersive signals we compute the median of the spectrogram PSD (with decibel scaling) as a function of time. We then run a peak finding routine and calculate prominence defined as the minimum vertical distance that the signal must descend on either side of the peak before either climbing back to a level higher than the peak. The air wave arrival time, t_{AW}, is given by the highest peak after subtracting a baseline value so that all peaks are positive valued and multiplying by their prominence. The importance of estimating the arrival time of the air wave is that it allows the unknown origin time, t_0, of the impulsive loading to be determined according to

$$t_0 = t_{AW} - \frac{x}{c_{air}} \tag{22}$$

The propagation distance, x, was determined by the GPS measured horizontal offset between source and microphone for artificial source calibration experiments. For cases where the source position was not known, such as natural icequakes, the propagation distance was estimated by iteration to maximise the fit with the dispersive chirp signal of

the ice flexural wave (see section 4.4).

4.4. Dispersive ice flexural wave chirp and range to source

When the dispersive chirp signal of the ice flexural wave was recorded by the microphone, we chose to use it to estimate the range to source, i.e., the horizontal offset between source and microphone, under the assumption that this corresponds to the flexural wave propagation distance, x (ignoring possible near field effects around the source). Iterating over possible values of x, we have proposed, tested and utilized the following procedure:

1. Set origin time, t_0, using Eq. (22).

For each frequency in the STFT define a time window with a length of five STFT time steps centred at the arrival time corresponding to the group velocity. For the plate in a vacuum model this is determined directly by Eq. (18), with ice thickness constrained by the air-coupled flexural wave as outlined in section 4.2. For the full model, both the frequency (Eq. (6)) and group velocity (Eq. (9)) are pre-computed in terms of wavenumber prior to the iteration over x. The group velocity at a given frequency is determined by spline interpolation along the curve linking the pre-computed frequencies and group velocities and the arrival time is given by $t(\omega) = x/v_g(\omega)$.

2. The mean of the decibel scaled PSD is extracted, at a given frequency, according to the temporal window centred at the arrival time corresponding to the group velocity of the ice flexural wave, multiplied by a triangular weight function.
3. The weighted-mean PSD is then averaged over the frequency axis of the STFT, excluding the range within ±10 Hz of the air-coupled flexural wave frequency to avoid interference.

The quantity derived by this procedure corresponds to a weighted average of the PSD following the chirp path in time-frequency space defined by the flexural wave group velocity, which physically corresponds to the arrival of the signal envelope of the dispersive ice flexural wave. The value of x is assumed to be that which maximises this quantity.

4.5. Air-coupled flexural wave overtones and finite plate boundary effect

Inharmonic overtones are a commonly encountered feature of the acoustic field corresponding to impulsively excited plates (e.g., Benade, 2012; Rossing, 2000). Importantly, the ratio of overtone to fundamental frequency is independent of the physical properties and fluid loading of the plate and depends only on the plate geometry, edge boundary conditions and vibrational mode (e.g., Benade, 2012; Crighton and Innes, 1983; Rossing, 2000). We estimated the expected overtone series by calculating the natural frequencies of thin plates in vacuum, whose geometry was traced according to the shapes of Langvannet, Storvatnet and Kråkskarvatnet, i.e., the frozen lakes where overtones were observed. We imposed a simply supported boundary condition (zero displacement along boundary) and calculated the natural frequencies and mode shapes by solving the homogeneous, partial-differential eigenvalue problem on the finite element meshed plates using the "Partial Differential Equation Toolbox" in MATLAB R2021a. We selected elastic properties and density corresponding to ice, but since the air and water above and below the ice were ignored the natural frequencies themselves are not of relevance, only their ratio with the fundamental frequency. The first ten overtones are listed in Table 1, in terms of their ratios to the fundamental frequency for each plate. The series of overtones are broadly similar for the three models, but we note that the overtone to fundamental frequency ratios differ noticeably due to the specific geometries of the three lakes. Illustrations of the mode shapes and mesh geometries for the three models are provided in Appendix A.

5. Results

The value of Young's modulus, E, assumed at each frozen lake was calibrated using drilled thicknesses according to Eq. (21) and the results are summarised in Fig. 3. At Langvannet, relatively uniform clear, black ice was observed following a stable cold period and the air temperature during the experiments was stable at ~−12 °C. Air-coupled flexural waves excited by both hammer strikes and jumping indicate $E \approx 9.8$ GPa (Fig. 3a), which is consistent with laboratory measurements on S2 columnar ice for temperatures ~−12 °C according to Sinha (1989). Clear black ice was also encountered at Storvatnet where the air temperature was ~−4 °C. We weight the results of the hammer strike experiments higher than the icequake measurements where the source position was not accurately constrained and assume $E = 9.7$ GPa (Fig. 3b) to be representative, which is also in line with S2 columnar ice at temperature ~−4 °C (Sinha, 1989). Icequake activity was likely related to increasing air temperatures and stream inflow under the ice causing flexure. At Kråkskarvatnet a thin layer of ice (~1 cm) above lenses of water above ~24 − 26 cm clear black ice (assumed to be columnar basal accumulated) was observed. The surface of the ice was relatively wet and soft. The air-temperature was ~−4 °C during the experiments, but the assumed representative value $E = 8$ GPa (Fig. 3c) reflects the softer and wetter ice that was observed due to a preceding warmer period and rain. Few hammer strikes successfully excited air-coupled flexural waves due to the thin upper ice layer and water lenses that made it difficult to strike the main ice layer. Despite this, we weighted the hammer strike experiments higher than the icequakes from varying source positions since ice thickness variation between source and microphone may affect the accuracy of E estimated from icequakes. The high level of icequake activity that was observed at Kråkskarvatnet was likely related to falling temperatures, freezing of water and/or differential thermal contraction cracking of the ~1 cm thick upper ice layer partially contacting the main ice layer around the perimeters of the water lenses.

The ice thicknesses estimated from air-coupled flexural wave frequencies according to Eq. (20) are shown in Fig. 4. In general, we found good agreement between thickness measured in holes drilled in the ice and those estimated with air-coupled flexural waves. We observe some spread in the estimates from Langvannet that we attribute to the relatively high levels of background noise due to human activity. The estimates corresponding to the thickest ice drilled at Kråkskarvatnet also depart from the ideal line of agreement, which is likely due to the challenging ice conditions where pools of partially re-frozen surface water may have influenced the physical sampling, flexural behaviour of the ice, or both.

Considering the different types of experiments that were conducted, we see that the air-coupled flexural wave is a surprisingly robust feature of impulsively excited lake ice. As shown in Fig. 5, we observe similar performance for different impulse types from hammer strikes, to

Table 1
Lowest overtone to fundamental frequency ratios for elementary plate geometries and boundary conditions.

Plate Shape	Edge condition	Overtone to fundamental frequency ratio									
Langvannet	simply supported	1.14	1.79	2.44	2.50	2.96	3.18	3.40	3.75	3.93	4.34
Storvatnet	simply supported	1.46	1.77	2.04	2.51	2.90	3.08	3.29	4.00	4.05	4.43
Kråkskarvatnet	simply supported	1.32	1.94	2.32	2.53	2.72	2.96	3.18	3.66	3.94	4.24

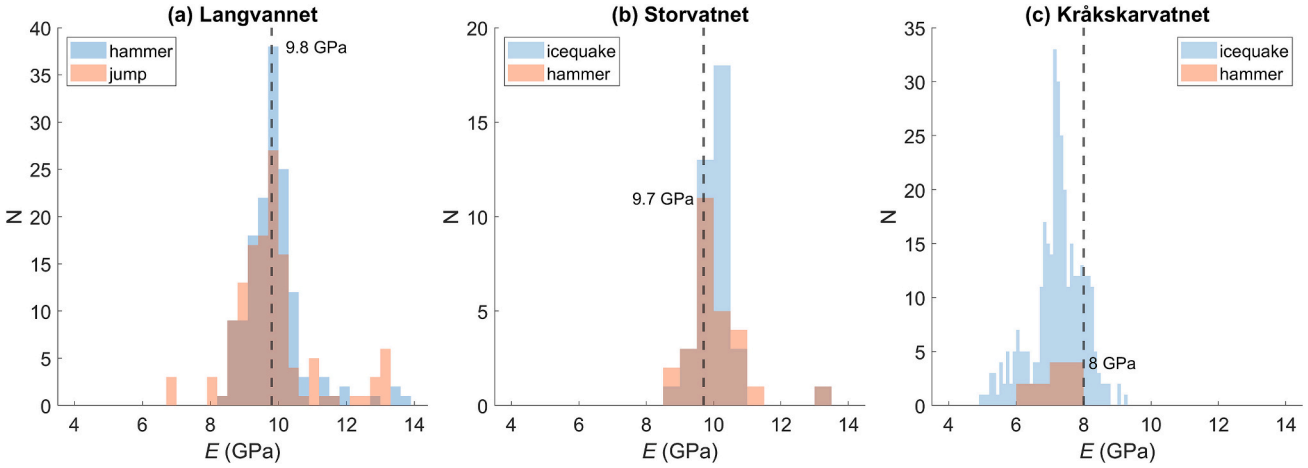

Fig. 3. Estimates of Young's modulus, E, based on air-coupled flexural wave frequencies constrained by ice thicknesses (Eq. (21)) measured in boreholes in the vicinity of the microphone. Dashed lines denote the constant values of 9.8 GPa, 9.7 GPa and 8 GPa that were assumed for subsequent ice thickness estimations, Eq. (20), at Langvannet, Storvatnet and Kråkskarvatnet, respectively.

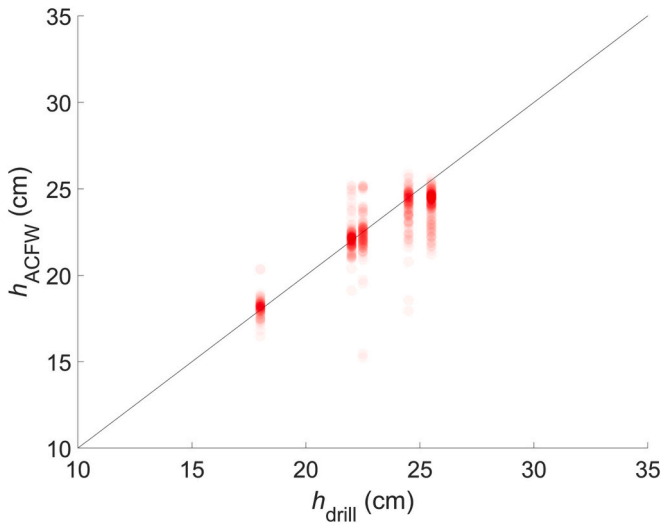

Fig. 4. Summary of ice thicknesses estimated by air-coupled flexural wave frequencies compared with drilled thicknesses in the vicinity of the microphone position for all source types (hammer, jump, ice skate, icequake) and all microphone positions (on ice, on land, handheld). The ice thickness was 18 cm in all three holes drilled at Storvatnet (28th November 2022), 22–22.5 cm in six holes drilled at Langvannet (23rd November 2022) and 24.5–25.5 cm in two holes drilled at Kråkskarvatnet (2nd December 2022). Individual estimates are transparent so that increased colour density represents repeated measurements.

jumping, or tapping with ice skates. We see a slight tendency to underestimation for the natural icequakes which may be related to their more distal position and some slight spatial variation in ice thickness leading to a path effect such that the air-coupled flexural wave corresponds to the ice thickness at some distance from the microphone. Fig. 5 also shows that the microphone recording of air-coupled flexural waves is relatively robust to the positioning of the microphone, whether it was placed on rocks along the shoreline (<1 m from the ice), resting on the ice with the microphone ~5 cm above the ice surface or held in hand with the microphone ~130 cm above the ice surface. By contrast, recording the dispersive ice flexural wave was quite sensitive to microphone position, being more attenuated when the microphone was held in hand or placed on land than when it was resting directly on ice. These features will be further illustrated with reference to specific data examples in the following sections.

5.1. Langvannet

At Langvannet a detailed series of controlled experiments were conducted, where the positions of hammer strike and jump impulsive sources as well as microphone position were constrained by GPS positioning so that the horizontal offset between source and microphone could be calculated. The results of these experiments with varying offset are shown in Fig. 6. We see that the air-coupled flexural wave estimates are most reliable for the larger offsets, >30–40 m, with greater spread at shorter offsets. This is because the duration of the air-coupled flexural wave, whose envelope travels at approximately twice the phase velocity of sound in air, increases with increasing offset and becomes progressively dispersed in time from the broadband air-wave that arrives after and the high-frequency part of the dispersive ice flexural wave that arrives before it. At shorter offsets the potential for interference between these wave modes increases and the short duration of the air-coupled flexural wave means that estimation of its monotonic frequency becomes progressively more difficult following Heisenberg's uncertainty principle. At very large offsets the performance of air-coupled flexural wave thickness estimation is also likely to decrease due to decaying flexural wave amplitudes and decreasing signal to noise ratio, but the profile shown in Fig. 6 was too short to show this effect.

Fig. 7 shows a hammer strike recorded at ~45 m offset, i.e., the range where the reliability of air-coupled flexural wave thickness estimation becomes very good (see Fig. 6). Since the microphone was resting on the ice, the dispersive ice flexural wave is easily discernible on the decibel scaled spectrogram (Fig. 7a), though note that the linearly scaled waveform remains dominated by the monochromatic air-coupled flexural wave (Fig. 7b). The thickness calculated from the air-coupled flexural wave agrees very well with the drilled thickness and the propagation distance giving best fit with the dispersive ice flexural wave agrees quite well with the offset between source and microphone measured by smartphone GPS (Fig. 7a), given that we may expect errors on the order of a couple of meters associated with these positions. We also found that the very simple plate in a vacuum model gave a reasonable approximation of the ice flexural wave, but the full model better fits the observed shape of the chirp signal. Two inharmonic overtones of the air-coupled flexural wave were clearly discernible on the spectrogram and the Thomson multitaper PSD, where several smaller spectral peaks are also visible (Fig. 7c). We were able to link the spectral peaks to specific natural modes of vibration of a finite plate modelled after the geometry of Langvannet. The strongest overtones correspond to mode shapes with vertical displacement of the same polarity along the path connecting the hammer strike and microphone

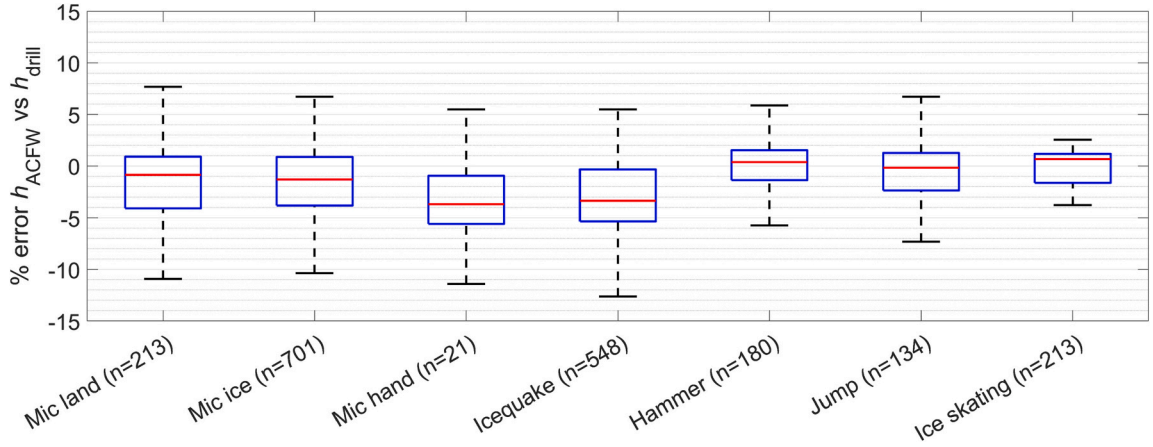

Fig. 5. Box and whisker plots summarising percent deviation of air-coupled flexural wave thickness estimates from thicknesses measured in boreholes in the vicinity of the microphone for different microphone positions; on land (along shoreline, mic ~5 cm above ground), on ice (mic ~5 cm above ice surface) and in hand (mic held ~130 cm above ice surface) and for different impulsive forces; natural icequakes, hammer strikes, jumps and tapping with ice skates. Red lines indicate medians, blue boxes indicate the 25th to 75th percentile range and *n* is the number of measurements for each category. (For interpretation of the references to colour in this figure legend, the reader is referred to the web version of this article.)

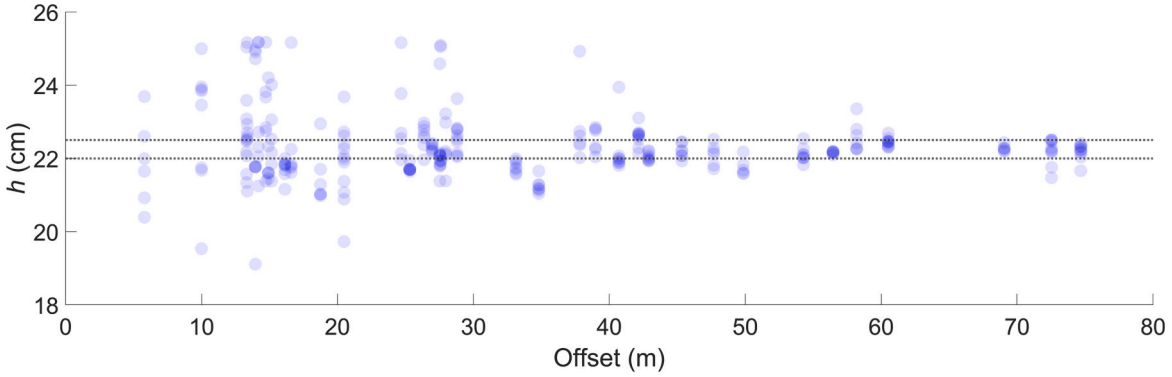

Fig. 6. Air-coupled flexural wave thickness estimates at Langvannet as a function of the horizontal offset between GPS positions of the microphone and impulsive load, consisting of hammer strikes and jumps, along a linear profile. Dotted lines show the range of ice thickness measured in six holes across the span of the profile.

positions (Fig. 7d-e).

5.2. Kråkskarvatnet

Fig. 8 shows an example of an icequake recorded at Kråkskarvatnet, where the microphone was held in hand at a height of ~130 cm above the ice. The dispersive ice flexural wave was strongly attenuated in this case but suggests the icequake occurred around 195 m away from the microphone (Fig. 8a). The air-coupled flexural wave has high amplitude and long duration as a result of the distal source position and the estimated ice thickness agrees perfectly with the drilled thickness in the vicinity of the microphone. A series of inharmonic overtones were also recorded and are clearly discernible in both spectrogram (Fig. 8a) and the Thomson multitaper PSD (Fig. 8c). Again, the recorded overtones agree well with natural modes of vibration predicted for a finite element model of Kråkskarvatnet (Fig. 8d,e,f). We note that the fourth natural mode (Fig. 8d) does not predict much vertical displacement at the microphone position, though we may infer that the source position ~200 m away corresponds to one of the displacement lobes predicted for this mode.

Fig. 9 shows an icequake recorded with the microphone placed on a boulder along the shoreline on the opposite side of Kråkskarvatnet to the example shown in Fig. 8. The dispersive ice flexural wave was less attenuated in this configuration (Fig. 9a), although the linearly scaled waveform is still dominated by the monochromatic air-coupled flexural wave. The smaller estimated propagation distance, ~67 m, may also contribute to the stronger dispersive ice flexural wave. The inharmonic overtone series corresponding to modelled natural modes of the finite plate (Fig. 9c-f) are quite similar to the example shown in Fig. 8, which leads us to speculate that the source position of the two icequakes might have been similar.

5.3. Storvatnet

Fig. 10 shows an example of an icequake recorded at Storvatnet with the microphone resting on rock along the shoreline. In this case the dispersive ice flexural wave was somewhat attenuated, but still visible on the decibel scaled spectrogram and suggests a source position ~175 m away from the microphone (Fig. 10a). As is typical, the linearly scaled waveform (Fig. 10b) is dominated by the monochromatic air-coupled flexural wave whose frequency gives an estimated ice thickness in excellent agreement with the drilled thickness in the vicinity of the microphone. We also observe inharmonic overtones at frequency ratios compared to the fundamental frequency that agree well with those predicted by the finite element model for a plate with the same geometry as Storvatnet (Fig. 10c).

A contrasting example is shown in Fig. 11, which was recorded at the opposite end of the lake where stream inflow and open water was observed adjacent to the shore. There was a lot of icequake activity in this area, likely related to the inflow of water under the ice creating

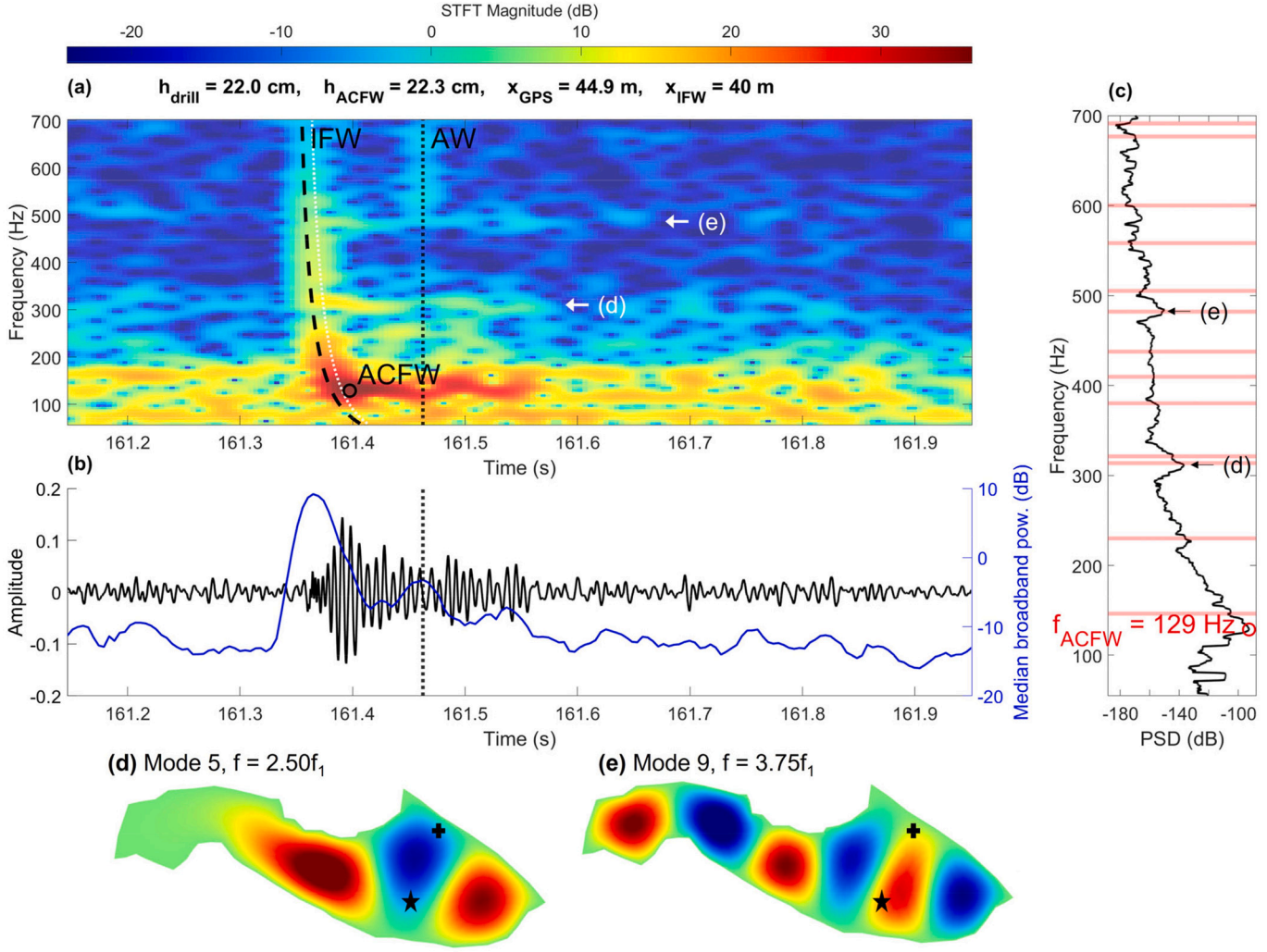

Fig. 7. A hammer strike at Langvannet recorded with microphone resting on ice. (a) Spectrogram annotated with different wave components: broadband air-wave (AW), monochromatic air-coupled flexural wave (ACFW) and dispersive ice flexural wave (IFW). ACFW was used to estimate ice thickness, h_{ACFW}, which is compared to drilled thickness, h_{drill}. IFW was used to estimate propagation distance, x_{IFW}, which is compared to GPS measured source-microphone offset, x_{GPS}. Dotted white line shows IFW arrival time for a plate in vacuum for comparison with full model (black dashed line). (b) Signal waveform recorded by microphone (black line) and median broadband power (blue line). (c) Thomson multitaper PSD annotated with air-coupled flexural frequency, f_{ACFW}, and overtone series (pink lines) predicted from finite element model. (d) and (e) illustrate the normalised vertical displacement of selected finite plate natural modes of vibration, where crosses indicate microphone position and stars indicate position of hammer strike for this recording.

upwards pressure and ice flexure. The air-coupled flexural wave also indicates the ice was considerably thinner in this area, consistent with the observation of open water nearby. With the microphone casing resting directly on the ice the chirp signal of the ice flexural wave is much stronger and is well resolved in the spectrogram (Fig. 11a). The overtones corresponding to the lowest natural modes of vibration of the modelled finite plate are also enhanced in this example, compared to the one shown in Fig. 10. This is likely because the microphone position for this example lies in the vicinity of the dominant deflection lobes for these modes. The enhanced amplitude of Mode 3 compared with Mode 2 (Fig. 11c) can also be understood in terms of the larger relative displacements predicted in the vicinity of the microphone position for Mode 3 (Fig. 11e) compared to Mode 2 (Fig. 11d).

6. Discussion

6.1. The flexural wavefield recorded by microphone

The experimental results presented in this study demonstrate that the flexural wavefield of a floating ice plate is dominated by the air-coupled flexural wave. The air-coupled flexural wave was shown to be recordable and similarly useful as an estimator of ice thickness for a variety of microphone positions and impulsive source types (Fig. 5). This result was largely in line with expectations based on the earlier study of Romeyn et al. (2021), but this study demonstrates that a simple microphone is a highly practical and accessible means of recording these waves. By contrast, it was a surprising result that the dispersive ice flexural wave was also recordable by a microphone, though it was significantly attenuated when the microphone was held in hand or placed on land. The dispersive ice flexural wave was strongest when the microphone casing was resting directly on the ice, with the microphone elements themselves ~5 cm above the ice. We expect that the vibrations of the dispersive flexural wave propagating in ice may either couple directly through contact between the microphone casing and ice or that the microphone may be picking up pressure waves in air corresponding to non-propagating evanescent waves whose amplitude decreases exponentially with distance from the surface. The detection of evanescent waves would be consistent with other studies involving near-ground microphones for the detection of landmines (Larson et al., 2007) and surface wave testing of pavements and soils (Rydén, 2010;

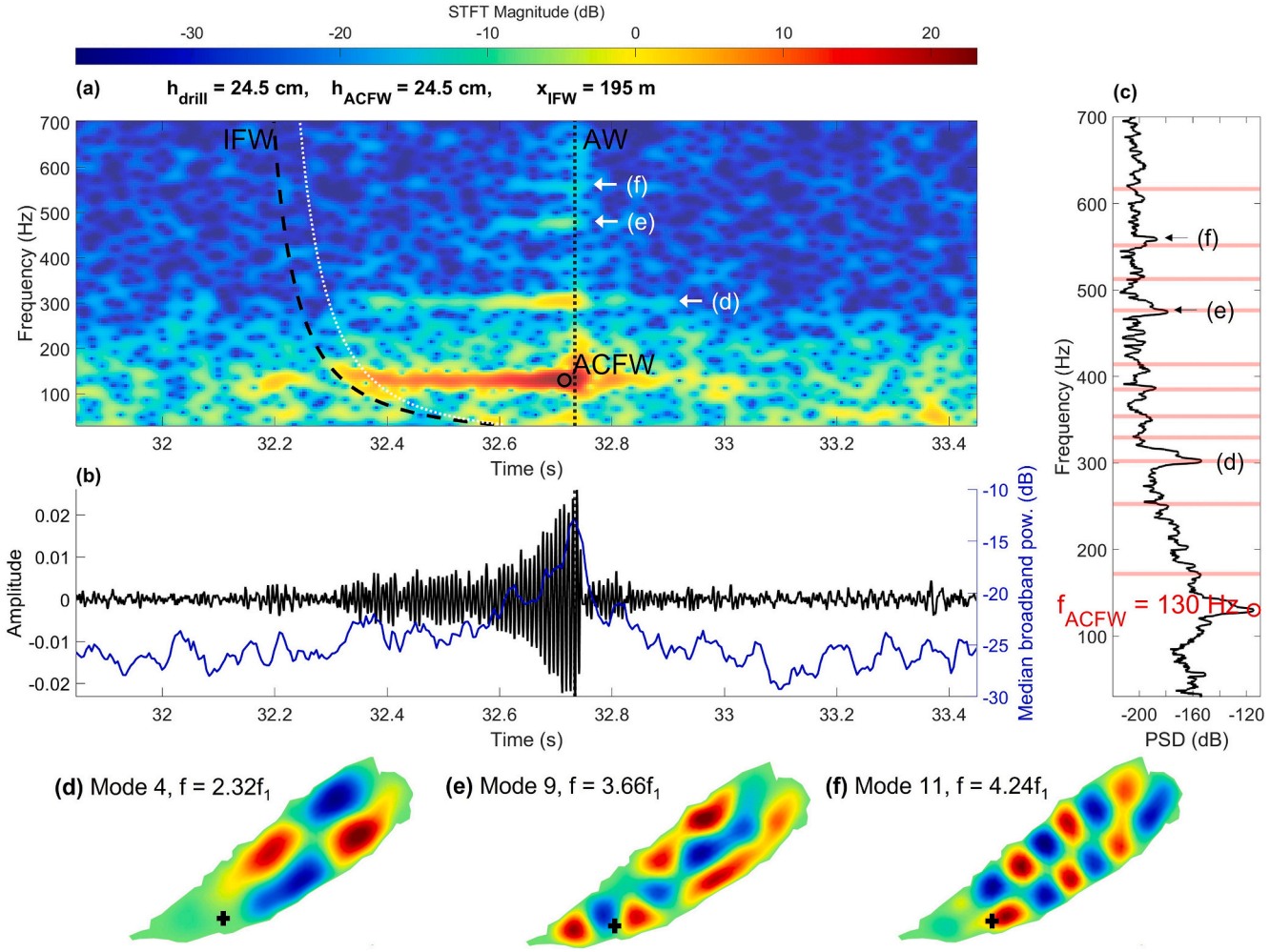

Fig. 8. An icequake at Kråkskarvatnet recorded by handheld microphone ~ 130 cm above ice. (a) Spectrogram annotated with different wave components: broadband air-wave (AW), monochromatic air-coupled flexural wave (ACFW) and dispersive ice flexural wave (IFW). ACFW was used to estimate ice thickness, h_{ACFW}, which is compared to drilled thickness, h_{drill}. IFW was used to estimate propagation distance, x_{IFW}. Dotted white line shows IFW arrival time for a plate in vacuum for comparison with full model (black dashed line). (b) Signal waveform recorded by microphone (black line) and median broadband power (blue line). (c) Thomson multitaper PSD annotated with air-coupled flexural frequency, f_{ACFW}, and overtone series (pink lines) predicted from finite element model. (d), (e) and (f) illustrate the normalised vertical displacement of selected finite plate natural modes of vibration, where crosses indicate microphone position for this recording.

Rydén et al., 2019). Repeat measurements with the microphone held in a suspension shock mount at the same height above the ice surface might help to distinguish between the two presently ambiguous cases of solid-solid coupling between ice and microphone casing and detection of evanescent pressure waves in air.

Another surprising result was that in some microphone recordings we observed a series of monochromatic tones at higher frequencies than the air-coupled flexural wave, whose synchronicity and similar duration led us to interpret as inharmonic overtones of the air-coupled flexural wave. We were able to confirm this hypothesis by matching the overtones with natural vibrations of finite plates with geometries modelled after the studied frozen lakes using finite element analysis. The good agreement between model and observations also indicates that the simply supported boundary condition is an appropriate representation of the boundary between ice and land around the perimeter of frozen lakes. Interestingly, the relative intensity of the overtones could largely be understood in terms of microphone and source position. Predominantly the lowest modes of vibration associated with vertical displacement at microphone and/or source position were recorded. While sophisticated array techniques have also been shown to have great utility (e.g. Moreau et al., 2020a; Serripierri et al., 2022), it is striking how much information about the physical lake ice system appears to be contained in the acoustic field recorded by a single, inexpensive and widely available microphone.

6.2. *Uncertainty of physical parameters*

Since the propagation of the air-coupled flexural wave depends on the ice flexural stiffness, it cannot be used to simultaneously constrain both thickness and elastic properties. Simultaneous constraint of thickness and elastic properties requires measurement of multiple wave modes as demonstrated by Moreau et al. (2020a) and Serripierri et al. (2022). Since we did not record the longitudinal and shear horizontal guided wave modes of the plate, we consider the thickness to be the only variable and assume the elastic properties and density to be constant. This is justifiable because both flexural stiffness (Eq. (1)) and bearing capacity approximated by instantaneous breakthrough load (Eq. (4)) depend most sensitively on the ice thickness. It is, however, useful to consider how our thickness estimates are affected by incorrect values of assumed parameters.

For a given air-coupled flexural frequency and varying the assumed elastic properties and density of the ice (compared with a reference case), we end up with estimates of ice thickness, h, and instantaneous breakthrough load, P, that also deviate from the reference case. This is

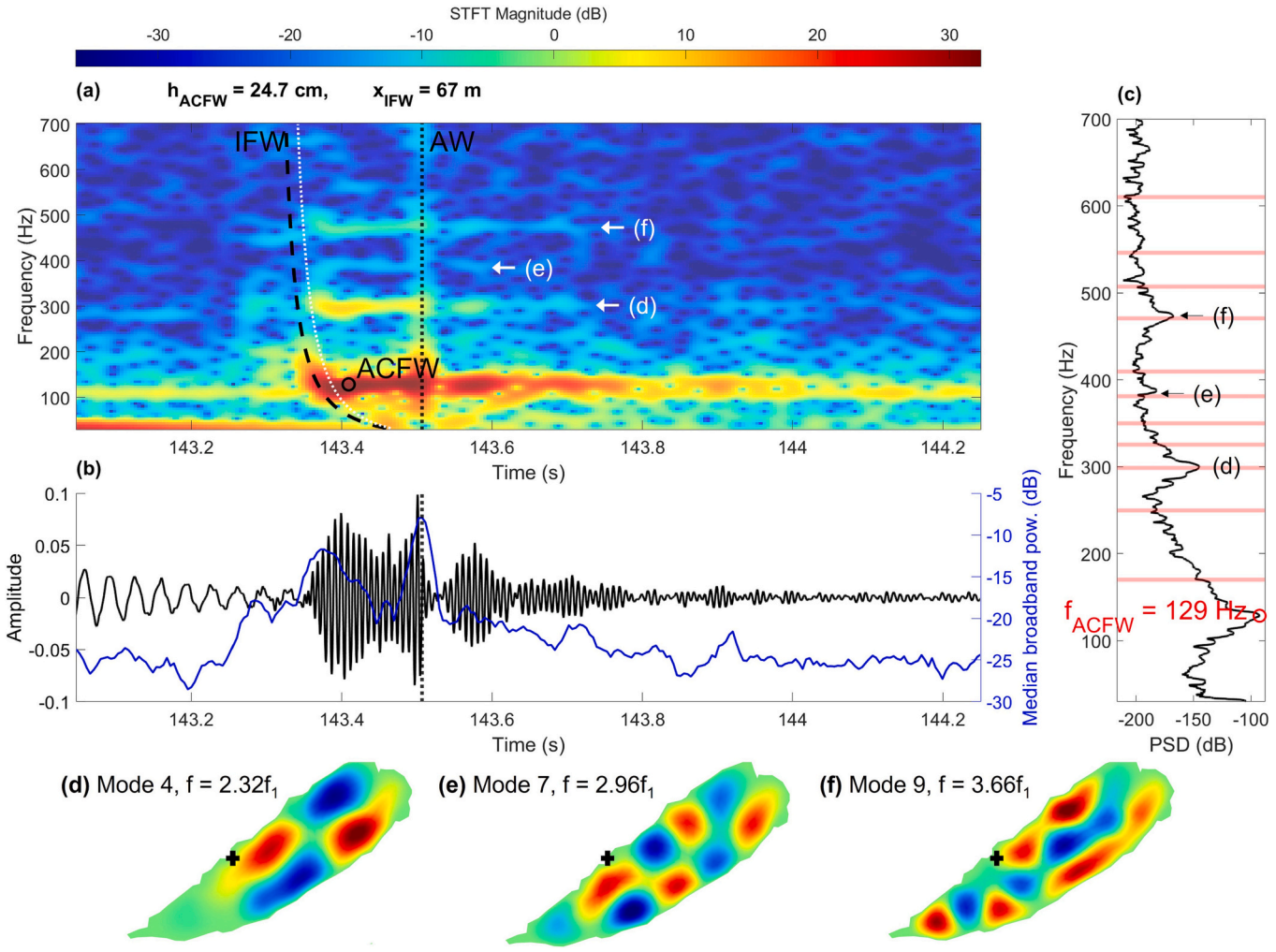

Fig. 9. An icequake at Kråkskarvatnet recorded by microphone on land, ~5 cm above boulder surface and ~ 1 m above the ice. (a) Spectrogram annotated with different wave components: broadband air-wave (AW), monochromatic air-coupled flexural wave (ACFW) and dispersive ice flexural wave (IFW). ACFW was used to estimate ice thickness, h_{ACFW}. IFW was used to estimate propagation distance, x_{IFW}. Dotted white line shows IFW arrival time for a plate in vacuum for comparison with full model (black dashed line). (b) Signal waveform recorded by microphone (black line) and median broadband power (blue line). (c) Thomson multitaper PSD annotated with air-coupled flexural frequency, f_{ACFW}, and overtone series (pink lines) predicted from finite element model. (d), (e) and (f) illustrate the normalised vertical displacement of selected finite plate natural modes of vibration, where crosses indicate microphone position for this recording.

shown in Fig. 12 for property ranges that are representative for those that could be expected for fresh water ice ranging from snow ice to columnar ice (Sinha, 1989; Traetteberg et al., 1975), although the range of Poisson's ratio is intentionally exaggerated compared to what one might expect in reality. The reference case, $\rho = 917$ kg m^{-3}, $\sigma = 0.31$, and $E = 9$ GPa, reflects a typical case of granular to columnar ice supported by laboratory measurements (Sinha, 1989) and our own calibration estimates (Fig. 3) using borehole thicknesses to constrain thickness and flexural waves to estimate E (Eq. (21)).

Fig. 12 shows that the thickness and bearing capacity estimated from air-coupled flexural waves is largely insensitive to the assumed Poisson's ratio, remaining within ~2% of the true value regardless of assumed value. Ice density also plays a very small role over the range anticipated for fresh water ice. The density plays a larger role in estimation of the bearing capacity, since plate buoyancy helps to support an applied load, but the largest expected errors are still ~2%. The assumed value of Young's modulus plays the most significant role, with 25% overestimation of thickness and 30% overestimation of bearing capacity error if Young's modulus is underestimated by 45%. Importantly, this case corresponds to mistaking columnar ice for snow ice and these are generally easy to distinguish on the basis of appearance, snow ice being white and columnar ice being clear/black or blue. Since we observed that the ice in this study was clear, we could limit the possible range to $8 \leq E \leq 10$ GPa, which would reduce the largest errors in derived parameters to ~5%. Since we also calibrated the assumed value of Young's modulus using borehole thickness measurements (Eq. (21)), we are confident that the assumed parameter values do not contribute to total errors of >5–10% in calculated thicknesses and instantaneous breakthrough loads. Incidentally, this is similar to the range of accuracy we see in practice when comparing estimated to drilled thickness in the vicinity of the microphone (see Fig. 5).

6.3. Implications for safe travel on ice

From Eq. (5), the critical ice thickness at which instantaneous breakthrough is expected to occur for a 100 kg load is 3.68 cm for columnar ice ($E = 9.7$ GPa, $\sigma = 0.31$) and 4.20 cm for snow ice ($E = 5.0$ GPa, $\sigma = 0.31$). These thicknesses agree quite well with the empirical experience of ice skaters (Ajne, 2013; Rankin, 2018), implying that elastic behaviour dominates over viscous creep for the thin ice and short loading times relevant to ice skating. We found that the air-coupled flexural wave is a surprisingly robust feature of the wavefield recorded by a microphone for ice subjected to various impulsive loadings, including tapping with ice skates, jumping, hammer blows or natural ice

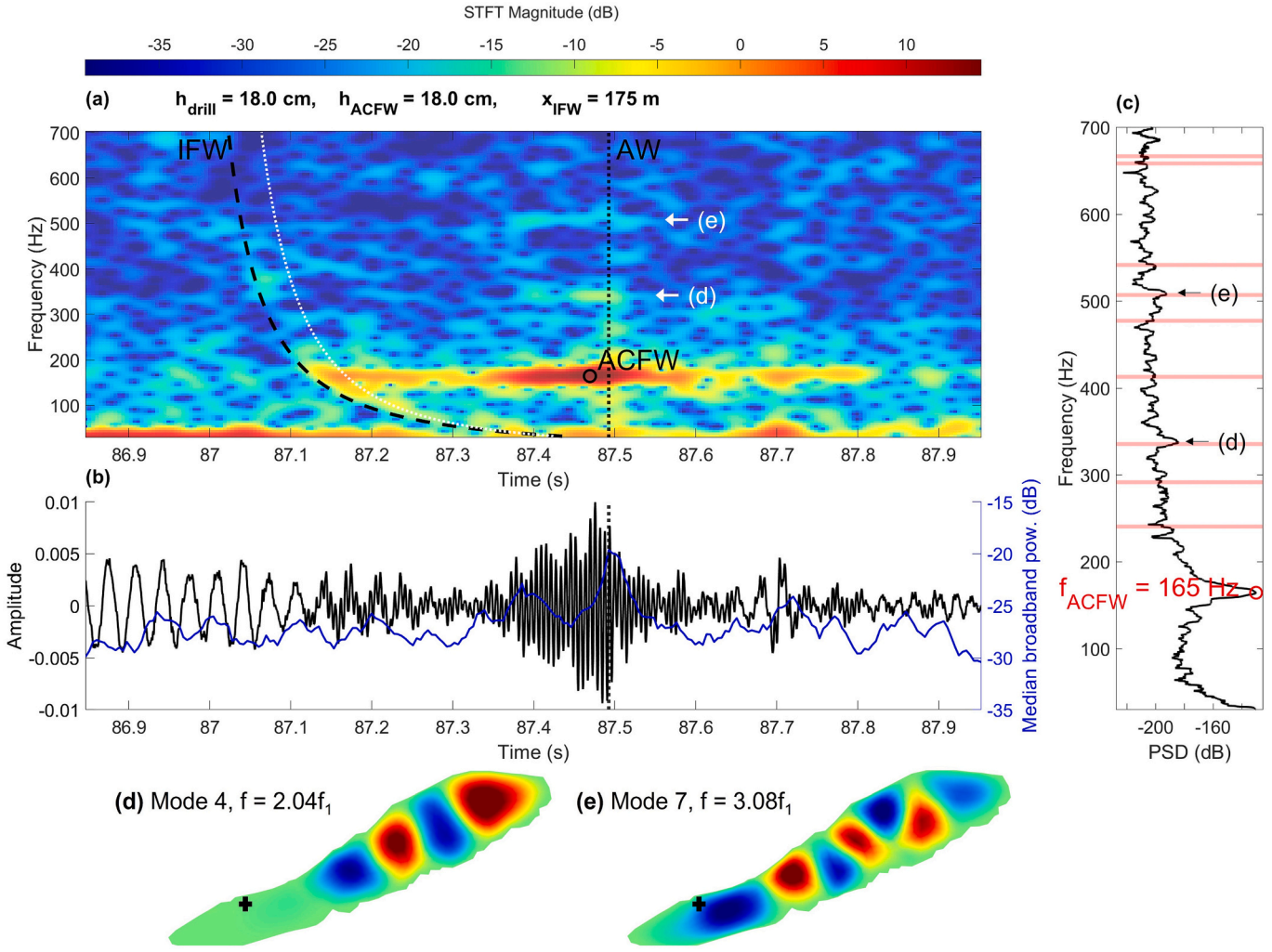

Fig. 10. An icequake at Storvatnet recorded by microphone on land, ~5 cm above the rock surface and ~ 1 m above the ice. (a) Spectrogram annotated with different wave components: broadband air-wave (AW), monochromatic air-coupled flexural wave (ACFW) and dispersive ice flexural wave (IFW). ACFW was used to estimate ice thickness, h_{ACFW}, which is compared to drilled thickness, h_{drill}. IFW was used to estimate propagation distance, x_{IFW}. Dotted white line shows IFW arrival time for a plate in vacuum for comparison with full model (black dashed line). (b) Signal waveform recorded by microphone (black line) and median broadband power (blue line). (c) Thomson multitaper PSD annotated with air-coupled flexural frequency, f_{ACFW}, and overtone series (pink lines) predicted from finite element model. (d), and (e) illustrate the normalised vertical displacement of selected finite plate natural modes of vibration, where crosses indicate microphone position for this recording.

quakes. Analysing the frequency of the air-coupled flexural wave recorded by a microphone in order to infer ice thickness is potentially easier and less time consuming than drilling through the ice to measure its thickness. It would, however, always be prudent to drill at least one hole to confirm the thickness and calibrate the assumed elastic parameters required to estimate the thickness with air-coupled flexural waves. Nonetheless, using a microphone to record air-coupled flexural waves appears to be a promising additional low-cost tool convenient enough that it could substantially increase the availability of timely and accurate information on ice thickness and thereby contribute to safer travel on floating ice.

7. Conclusion

A series of experiments conducted on three frozen lakes in the Tromsø region of Northern Norway show that the air-coupled flexural wave is a robust feature of the acoustic wavefield recorded by a microphone when the ice is impulsively loaded. We found that estimated ice thickness was reliably within 5–10% of the thickness measured in holes drilled in the vicinity of the microphone, regardless of whether the microphone was resting on the ice, was placed on land along the shoreline, or was handheld. Thickness estimation was also similarly accurate for a range of artificial sources including hammer strikes, jumps and tapping with ice skates. A slight tendency to underestimation of ice thickness for air-coupled flexural waves from natural icequakes may indicate a source to microphone path effect such that thickness measured in the vicinity of the microphone differs from the thickness dictating flexural wave propagation. The dispersive ice flexural wave was recorded in many cases where the microphone was resting on ice and was significantly attenuated when the microphone was handheld or positioned on land. The dispersive chirp signal of the ice flexural wave was used to estimate the flexural wave propagation distance, effectively the range to source. We also recorded inharmonic overtones that are analogous to the acoustics of drums and percussion instruments. We were able to demonstrate that the ratios of overtone to fundamental frequency varies for the three frozen lakes and are governed by the geometry of the lakes and the lateral boundary condition, which our results suggest can be reasonably approximated as simply supported. Since continuous ice of sufficient thickness is the main requirement to support a given load, improving the availability of accurate and timely

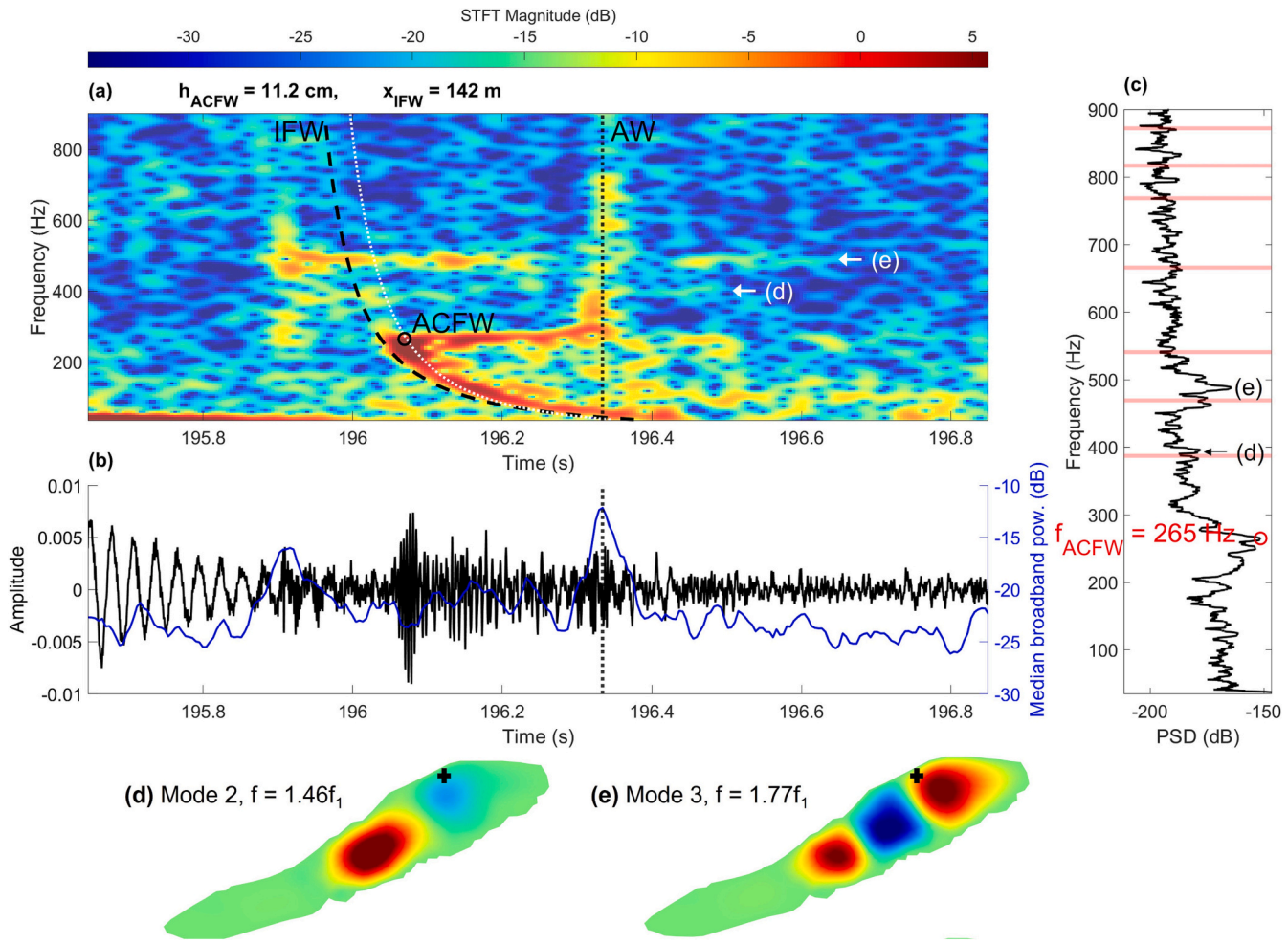

Fig. 11. An icequake at Storvatnet recorded by microphone resting on ice, ~5 cm above the surface near an area of with stream inflow, open water and thin ice observed near the shore. (a) Spectrogram annotated with different wave components: broadband air-wave (AW), monochromatic air-coupled flexural wave (ACFW) and dispersive ice flexural wave (IFW). ACFW was used to estimate ice thickness, h_{ACFW}. IFW was used to estimate propagation distance, x_{IFW}. Dotted white line shows IFW arrival time for a plate in vacuum for comparison with full model (black dashed line). (b) Signal waveform recorded by microphone (black line) and median broadband power (blue line). (c) Thomson multitaper PSD annotated with air-coupled flexural frequency, f_{ACFW}, and overtone series (pink lines) predicted from finite element model. (d), and (e) illustrate the normalised vertical displacement of selected finite plate natural modes of vibration, where crosses indicate microphone position for this recording.

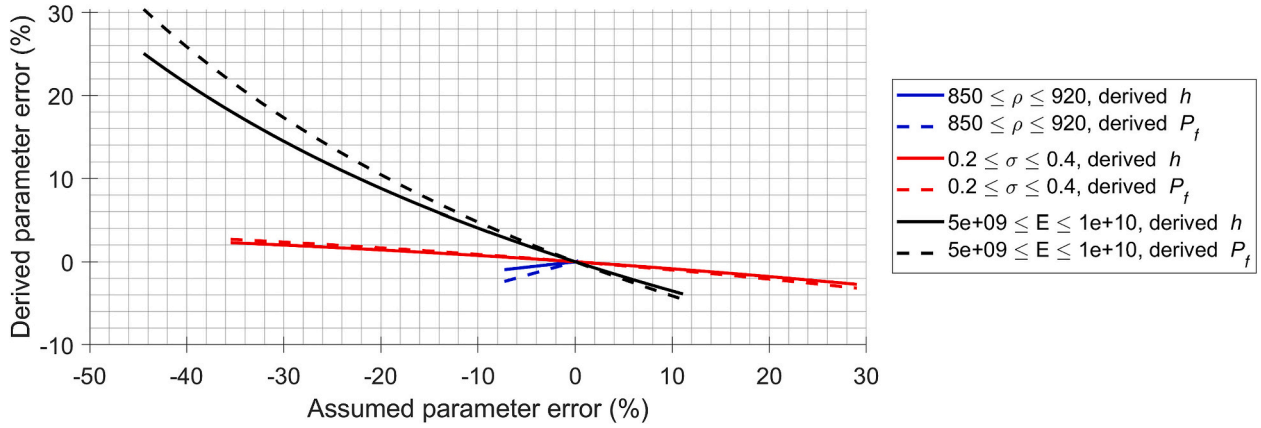

Fig. 12. Variation in derived ice thickness, h, (Eq. 20) and instantaneous breakthrough load, P_f, (Eq. 4) for varying assumptions of ice density ρ, Poisson's ratio σ, and Young's modulus E compared to a reference case with $\rho = 917\ kgm^{-3}$, $\sigma = 0.31$, and $E = 9$ GPa corresponding to typical fresh water ice (e.g. Sinha, 1989).

information on ice thickness has the potential to promote safe travel on floating ice. The results of this study underline the fact that a simple microphone is a surprisingly capable, widely available and convenient tool that can be used to estimate lake ice thickness and contribute to safer travel on floating ice.

Financial support

This research did not receive any specific grant from funding agencies in the public, commercial, or not-for-profit sectors.

CRediT authorship contribution statement

Rowan Romeyn: Conceptualization, Methodology, Formal analysis, Investigation, Data curation, Writing – original draft, Writing – review & editing, Visualization. **Alfred Hanssen:** Conceptualization, Methodology, Writing – original draft, Supervision.

Declaration of Competing Interest

The authors declare that they have no known competing financial interests or personal relationships that could have appeared to influence the work reported in this paper.

Data availability

The raw data acquired in this study is freely available via the UiT Open Research Data repository https://doi.org/10.18710/C2ONEX

Appendix A. Finite element analysis

The finite element meshes illustrated in Fig. A1 were constructed to reflect the peripheral geometry of the real frozen lakes where overtones of the air-coupled flexural wave were observed. The natural frequencies of these plates embedded in a vacuum medium were found by finite element modal structural analysis and the ratio of modal frequency to fundamental frequency was calculated. The mode shapes and frequency ratios of the first 12 modes are shown in Fig. A2 for the Langvannet model, Fig. A3 for the Storvatnet model and Fig. A4 for the Kråkskarvatnet model.

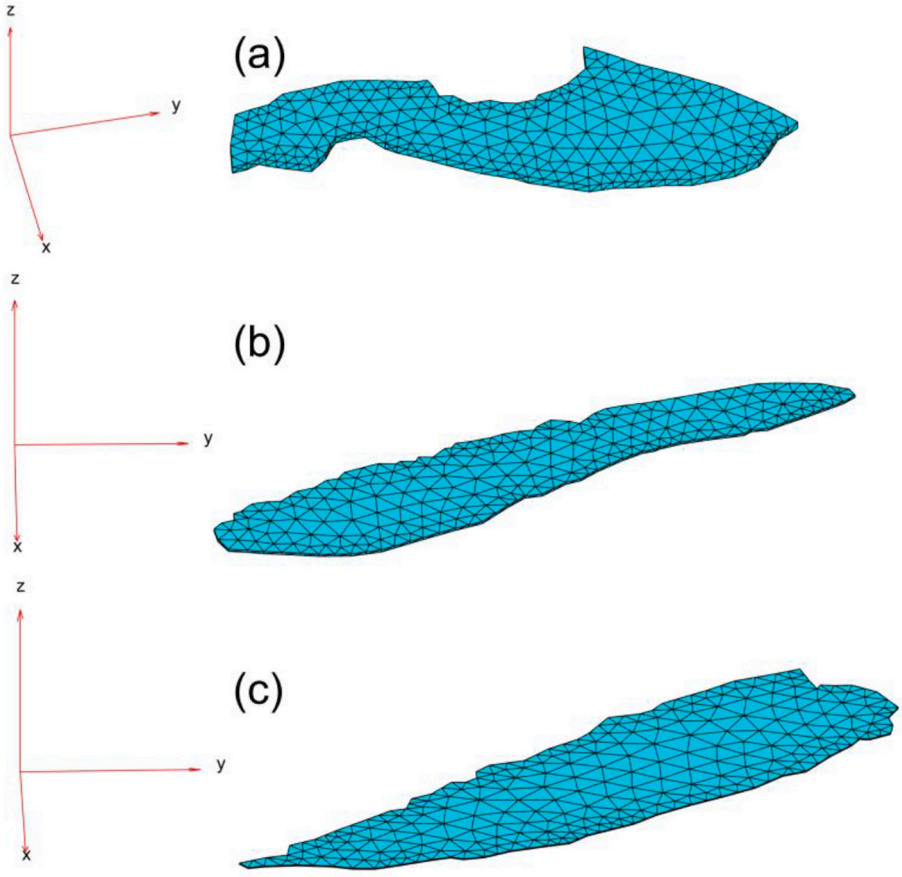

Fig. A1. Illustration of the finite element meshes with quadratic tetrahedral elements whose perimeter geometry models (a) Langvannet, (b) Storvatnet and (b) Kråkskarvatnet, i.e., the frozen lakes on Kvaløya, Norway where overtones of the air-coupled flexural wave were observed.

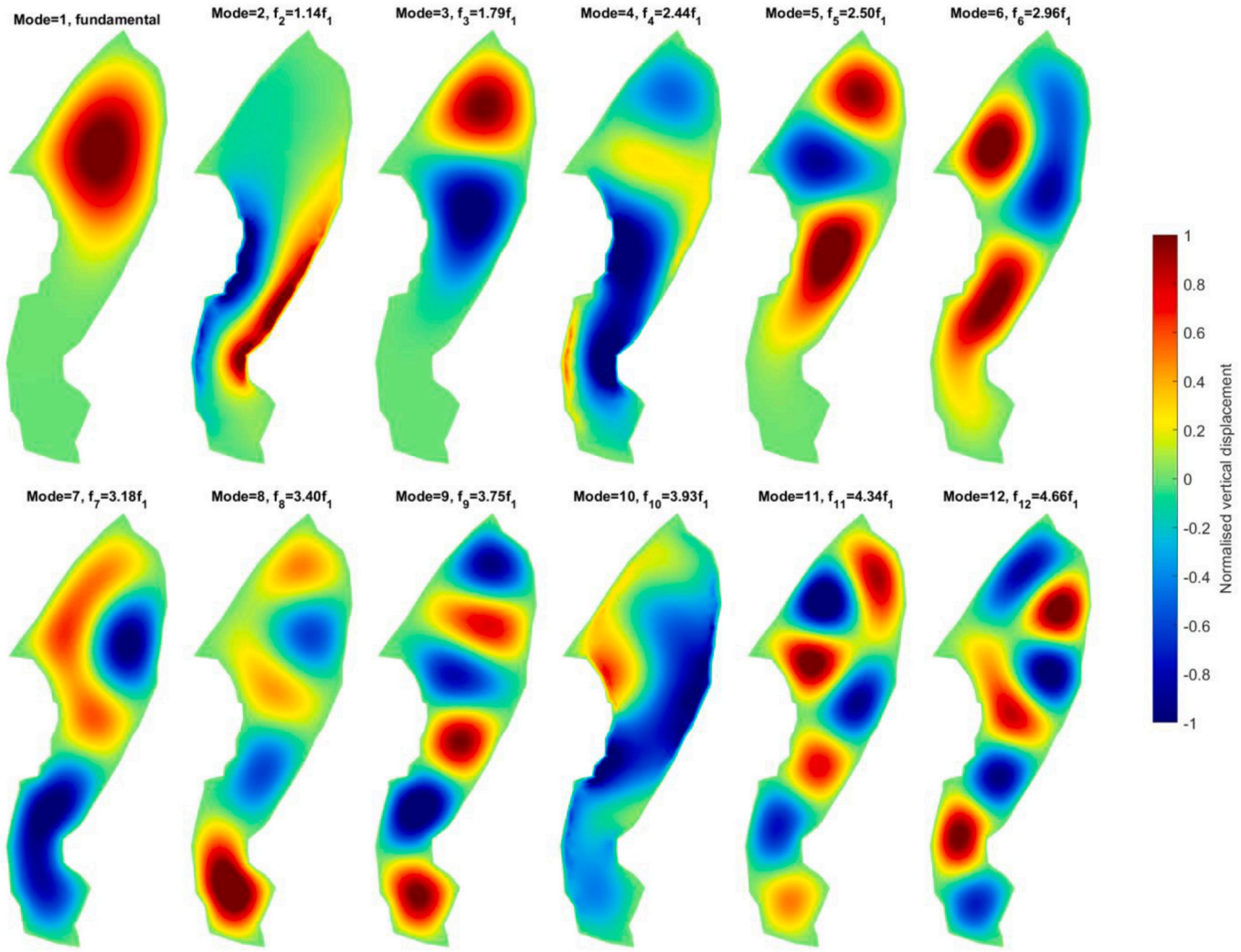

Fig. A2. Transverse displacement mode shapes of the 12 lowest natural modes of a finite element model approximating the geometry of the lake, Langvannet on Tromsøya, Norway. The mode shapes are shown in plane view, viewed from above.

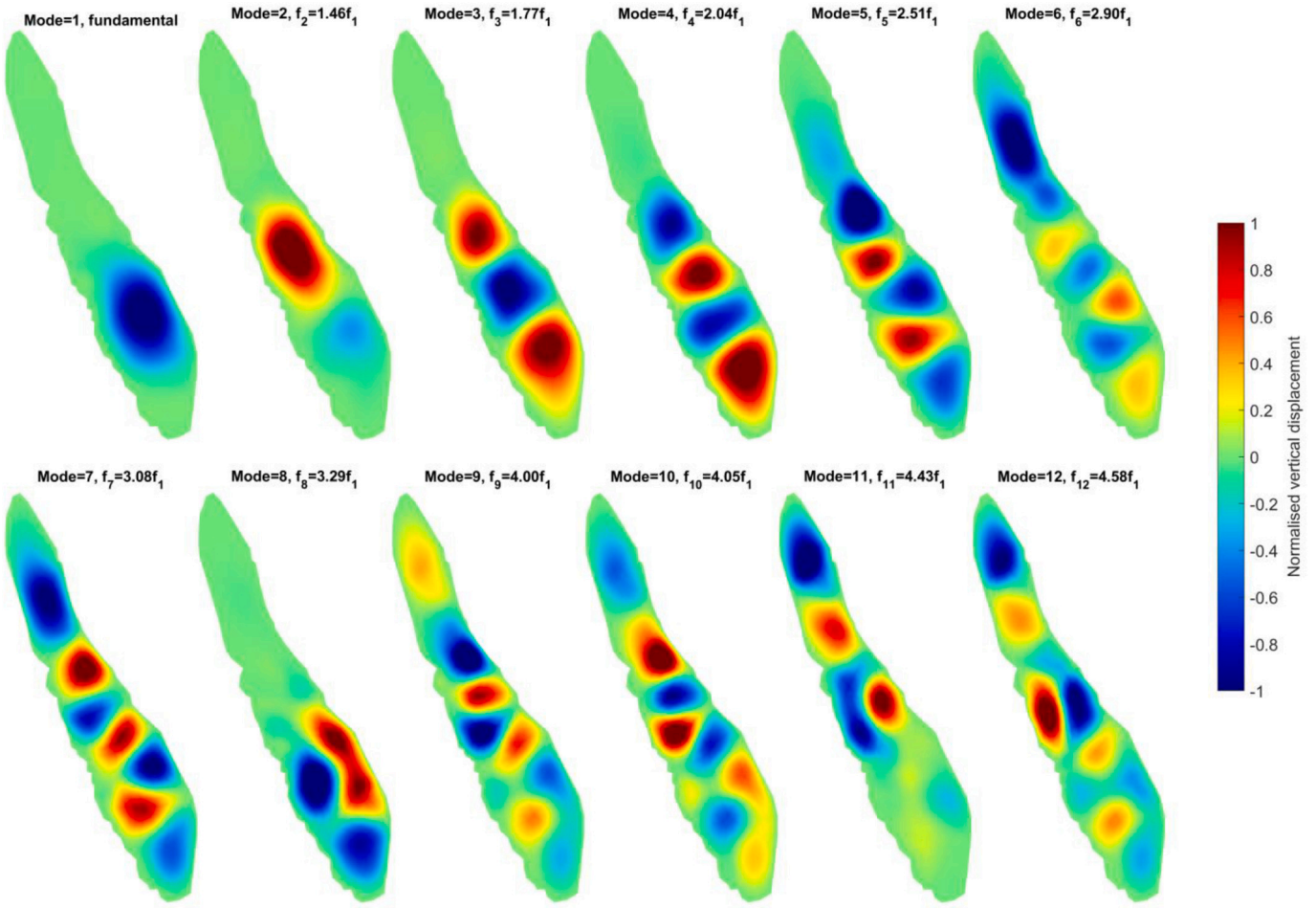

Fig. A3. Transverse displacement mode shapes of the 12 lowest natural modes of a finite element model approximating the geometry of the lake, Storvatnet on Kvaløya, Norway. The mode shapes are shown in plane view, viewed from above.

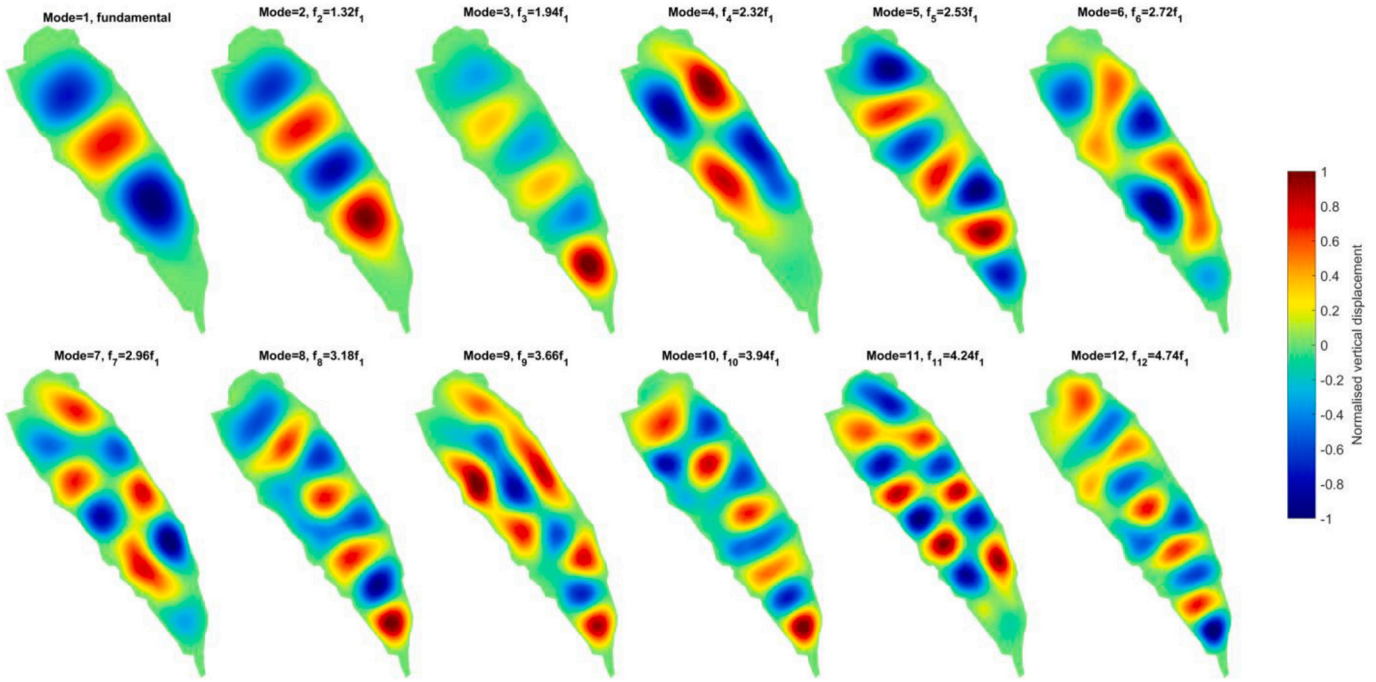

Fig. A4. Transverse displacement mode shapes of the 12 lowest natural modes of a finite element model approximating the geometry of the lake, Kråkskarvatnet on Kvaløya, Norway. The mode shapes are shown in plane view, viewed from above.

References

Ajne, M., 2013. Ice Physics for Recreational Ice-users: some thermal and Mechanical Properties of Natural Ice Covers. Publit. 1, 1–168. https://books.google.no/books?id=sxDBDAEACAAJ.

Beltaos, S., 1978. A strain energy criterion for failure of floating ice sheets. Can. J. Civ. Eng. 5 (3), 352–361. https://doi.org/10.1139/l78-040.

Beltaos, S., 2002. Collapse of floating ice covers under vertical loads: test data vs. theory. Cold Reg. Sci. Technol. 34 (3), 191–207. https://doi.org/10.1016/S0165-232X(02)00004-6.

Benade, A.H., 2012. Fundamentals of Musical Acoustics: Second, Revised Edition (2nd ed.). Dover Publications. https://books.google.no/books?id=0E0LHSXU0foC.

Bjurström, H., Rydén, N., 2019. Non-contact rolling surface wave measurements on asphalt concrete. Road Mater. Pavement Design 20 (2), 334–346. https://doi.org/10.1080/14680629.2017.1390491.

Crighton, D.G., Innes, D., 1983. Low frequency acoustic radiation and vibration response of locally excited fluid-loaded structures. J. Sound Vib. 91 (2), 293–314. https://doi.org/10.1016/0022-460X(83)90903-3.

Ewing, M., Crary, A., 1934. Propagation of elastic waves in ice, Part II. Physics 5 (7), 181–184.

Greenhill, A., 1886. Wave motion in hydrodynamics. Am. J. Math. 62–96.

Hanssen, A., 1997. Multidimensional multitaper spectral estimation. Signal Process. 58 (3), 327–332.

Harb, M.S., Yuan, F.-G., 2018. Air-coupled nondestructive evaluation dissected. J. Nondestruct. Eval. 37 (3), 1–19.

Hayley, D., Proskin, S., Ryder, R., Cislo, R., Baehl, F., Girard, E., Flaherty, W., Lozinsky, B., McManus, K., Tait, A., Warren, R., Fitzgerald, A., 2013. Best Practice for Building and Working Safely on Ice Covers in Alberta. Alberta Government, Work Safe Alberta. https://open.alberta.ca/dataset/sh010/resource/74decde6-8120-46be-b137-158bb63ee569.

Kerr, A.D., 1976. The Bearing Capacity of floating Ice Plates Subjected to Static or Quasi-Static Loads. J. Glaciol. 17 (76), 229–268. https://doi.org/10.3189/S0022143000013575.

Kinsler, L.E., Frey, A.R., Coppens, A.B., Sanders, J.V., 2000. Fundamentals of Acoustics, 4th Edition ed. John Wiley & Sons.

Larson, G.D., Martin, J.S., Jr., W. R. S, 2007. Investigation of microphones as near-ground sensors for seismic detection of buried landmines. J. Acoust. Soc. America 122 (1), 253–258. https://doi.org/10.1121/1.2743155.

Marsan, D., Weiss, J., Larose, E., Métaxian, J.-P., 2012. Sea-ice thickness measurement based on the dispersion of ice swell. J. Acoust. Soc. America 131 (1), 80–91. https://doi.org/10.1121/1.3662051.

Masterson, D., 2009. State of the art of ice bearing capacity and ice construction. Cold Reg. Sci. Technol. 58 (3), 99–112.

Moreau, L., Boué, P., Serripierri, A., Weiss, J., Hollis, D., Pondaven, I., Vial, B., Garambois, S., Larose, É., Helmstetter, A., 2020a. Sea ice thickness and elastic properties from the analysis of multimodal guided wave propagation measured with a passive seismic array. J. Geophys. Res. Oceans 125 (4) e2019JC015709.

Moreau, L., Weiss, J., Marsan, D., 2020b. Accurate estimations of sea-ice thickness and elastic properties from seismic noise recorded with a minimal number of geophones: from thin landfast ice to thick pack ice. J. Geophys. Res. Oceans 125 (11) e2020JC016492.

NVE, 2023. Ice accidents and incidents (original text in Norwegian: Isulykker og hendelser). Norwegian Water Res. Energ. Directorate 2023 (4/01/2023). https://www.varsom.no/ulykker/isulykker-og-hendelser/.

Nziengui-Bâ, D., Coutant, O., Moreau, L., Boué, P., 2022. Measuring the thickness and Young's modulus of the ice pack with DAS, a test case on a frozen mountain lake. Geophys. J. Int. https://doi.org/10.1093/gji/ggac504.

Press, F., Crary, A., Oliver, J., Katz, S., 1951. Air-coupled flexural waves in floating ice. EOS Trans. Am. Geophys. Union 32 (2), 166–172.

Rankin, A., 2018. How Skating on Thin Ice creates Laser-like sounds. Natl. Geogr. Retrieved 16.06.2020, from https://www.nationalgeographic.com/adventure/activities/winter-sports/skating-thin-black-ice-creates-sound-nordic-spd/.

Romeyn, R., Hanssen, A., Ruud, B.O., Johansen, T.A., 2021. Sea ice thickness from air-coupled flexural waves. Cryosphere 15 (6), 2939–2955. https://doi.org/10.5194/tc-15-2939-2021.

Rossing, T.D., 2000. Science of Percussion Instruments. World Scientific. https://doi.org/10.1142/4294.

Rydén, N., 2010. Towards non-contact surface wave testing of subsonic soil layers using microphones. In: GeoFlorida 2010, pp. 1389–1393. https://doi.org/10.1061/41095(365)139.

Rydén, N., Starkhammar, J., Yilmaz, Ö., Bjurström, H., Gudmarsson, A., Tofeldt, O., 2019. Small scale seismic testing using microphones. In: Fifth International Conference on Engineering Geophysics, Al Ain, UAE, 21–24 October 2019, pp. 44–47. https://doi.org/10.1190/iceg2019-011.1.

Serripierri, A., Moreau, L., Boue, P., Weiss, J., Roux, P., 2022. Recovering and monitoring the thickness, density, and elastic properties of sea ice from seismic noise recorded in Svalbard. Cryosphere 16 (6), 2527–2543. https://doi.org/10.5194/tc-16-2527-2022.

Sinha, N.K., 1989. Elasticity of natural types of polycrystalline ice. Cold Reg. Sci. Technol. 17 (2), 127–135.

Sinha, N.K., Cai, B., 1996. Elasto-Delayed-Elastic simulation of short-term deflection of fresh-water ice covers. Cold Reg. Sci. Technol. 24 (2), 221–235. https://doi.org/10.1016/0165-232X(95)00004-U.

Sodhi, D.S., 1995. Breakthrough Loads of floating Ice Sheets. J. Cold Reg. Eng. 9 (1), 4–22. https://doi.org/10.1061/(ASCE)0887-381X(1995)9:1(4).

Squire, V., Hosking, R.J., Kerr, A.D., Langhorne, P., 1996. Moving Loads on Ice Plates, vol. 45. Springer Science & Business Media.

Thomson, D.J., 1982. Spectrum estimation and harmonic analysis. Proc. IEEE 70 (9), 1055–1096.

Timco, G.W., Weeks, W.F., 2010. A review of the engineering properties of sea ice. Cold Reg. Sci. Technol. 60 (2), 107–129. https://doi.org/10.1016/j.coldregions.2009.10.003.

Traetteberg, A., Gold, L.W., Frederking, R., 1975. The strain rate and temperature dependence of Young's modulus of ice. In: Proc., IAHR 3rd Int. Symp. On Ice Problems, International Association for Hydro-Environment Engineering and Research (IAHR), pp. 479–486.

Yang, T.C., Yates, T.W., 1995. Flexural waves in a floating ice sheet: Modeling and comparison with data. J. Acoust. Soc. America 97 (2), 971–977. https://doi.org/10.1121/1.412076.

Zhu, J., 2008. Non-contact NDT of Concrete Structures Using Air Coupled Sensors (vols. Report No. NSEL-010). (NSEL Report Series, Issue). Newmark Structural Engineering Laboratory. University of Illinois at Urbana.